Crystal structure, thermal expansivity and elasticity of OH-chondrodite: Trends among dense hydrous magnesium silicates

Yu Ye[*1, 2], Steven D. Jacobsen[3], Zhu Mao[4], Thomas S. Duffy[5], Sarah M. Hirner[2], Joseph R. Smyth[2]

[1]*State Key Laboratory of Geological Processes and Mineral Resources, China University of Geosciences, Wuhan, Hubei 430074, P.R.China*

[2]*Department of Geological Sciences, University of Colorado, Boulder, CO 80309, USA*

[3]*Department of Earth and Planetary Sciences, Northwestern University, Evanston, IL 60208, USA*

[4]*School of Earth and Space Sciences, University of Science and Technology of China, Hefei, Anhui 230026, P.R.China*

[5]*Department of Geosciences, Princeton University, Princeton, NJ08544, USA*

*: corresponding author email: zylzylyeyu@gmail.com.

Abstract: We report the structure and thermoelastic properties of OH-chondrodite. The sample was synthesized at 12 GPa and 1523 K, coexisting with hydroxyl-clinohumite and hydrous olivine. The Fe content Fe/(Fe+Mg) is 1.1 mol%, and the monoclinic unit-cell parameters are: a = 4.7459(2) Å, b = 10.3480(7) Å, c = 7.9002(6) Å, α = 108.702(7)°, and V = 367.50(4) Å^3. At ambient conditions the crystal structure was refined in space group $P2_1/b$ from 1915 unique reflection intensities measured by single-crystal x-ray diffraction. The volume thermal expansion coefficient was measured between 150 and 800 K, resulting in $\alpha_V = 2.8(5)\times10^{-9}(K^{-2})\times T + 40.9(7)\times10^{-6}(K^{-1}) - 0.81(3)(K)/T^2$, with an average value of $38.0(9)\times10^{-6}$ K^{-1}. Brillouin spectroscopy was used to measure a set of acoustic velocities from which all thirteen components (C_{ij}) of the elastic tensor were determined. The Voigt-Reuss-Hill average of the moduli yield for the adiabatic bulk modulus, K_{S0} = 117.9(12) GPa, and for shear modulus, G_0 = 70.1(5) GPa. The Reuss bound on the isothermal bulk modulus (K_{T0}) is 114.2(14) GPa. From the measured thermodynamic properties, the Grüneisen parameter (γ) is calculated to be 1.66(4). Fitting previous static

compression data using our independently measured bulk modulus (isothermal Reuss bound) as a fixed parameter, we refined the first pressure derivative of the bulk modulus, K_T' = 5.5(1). Systematic trends between H_2O content and physical properties are evaluated among dense hydrous magnesium silicate (DHMS) phases along the forsterite-brucite join.

Keywords: chondrodite, dense hydrous magnesium silicates, crystal structure, thermal expansivity, bulk modulus, Grüneisen parameter

Introduction:

The dense hydrous magnesium silicate (DHMS) minerals along the brucite-forsterite join include phase A, norbergite, chondrodite, humite, and clinohumite (*Fig. 1*) as well as other DHMS minerals in the peridotite system. Among these phases, phase A, chondrodite, and clinohumite have been observed as dehydration products of serpentine as well as in experiments on MgO-SiO_2-H_2O systems at pressures of 5~12 GPa (Berry and James 2001; Smyth et al. 2006; Wunder 1998). These phases could serve as H_2O carriers in the Earth's upper mantle and transition zone. Due to the critical role of water in controlling silicate phase relations and physical properties at upper mantle conditions, the crystal structures and physical properties of DHMS have been extensively studied (e.g. Angel et al. 2001; McGetchin et al. 1970; Kanzaki 1991; Faust and Knittle 1994; Irifune et al. 1998; Kawamoto 2006; Komabayashi and Omori 2006; Ohtani et al. 2000; Sanchez-Valle et al. 2006; Shieh et al. 2000; Wunder et al. 1995; Ye et al. 2013). The composition and various thermoelastic properties of phase A, chondrodite, and clinohumite are summarized in *Table 1*.

The humite minerals are found in metamorphosed limestones and dolomites and contain variable proportions of F and OH (Friedrich et al. 2002). Variable Ti and F/OH humites are also known in high-pressure ultramafic rocks (Evans and Trommsdorff 1983) as well as being recently described in a serpentinized wehrlite (Shen et al. 2014). Within kimberlites, mineral associations including humites have indicated equilibrium pressures in excess of 6 GPa (Taskaev and Ilupin 1990). Synthetic hydroxyl-chondrodite (nominally $Mg_5Si_2O_{10}H_2$) is stable up to at least 12 GPa at temperatures below 1473 K (Burnley and Navrotsky 1996), and Fe-Ti-bearing compositions bracket the stability fields of chondrodite and clinohumite in typical mantle compositions (Khodyrev et al. 1992). Fluorine may significantly increase its thermal stability (Engi and Lindsley 1980) and incompressibility (Friedrich et al. 2002), but the estimated concentration of fluorine in the upper mantle is limited (e.g. McDonough and Sun 1995). Hence, the geological occurrence of chondrodite may be restricted to low-temperature regimes such as cold, subducting slabs and the mantle wedge above them.

The crystal structure of chondrodite is illustrated in *Fig. 2*. The structure is monoclinic (space group $P2_1/b$, *a*-unique). The non-conventional setting of space group $P2_1/c$ can be chosen to preserve the association with the *a*- and *b*-axes of olivine. In the crystal structure of OH-chondrodite, there are three distinct (Mg,Fe)-O_6 octahedra (M1, M2 and M3) and one Si-O_4 tetrahedron (Si). The ratio of M1 : M2 : M3

: Si equals 1 : 2 : 2 : 2, since the M1 sites are fixed at the special position of (1/2, 0, 1/2). Hydrogen atoms are bonded to O5 sites, which are also the positions for F anions in natural F-bearing samples. Thermoelastic properties of DHMS phases along the olivine-brucite join have been reported for a range of compositions (with variable H_2O, Fe, Ti, F, etc.) including thermal expansivity (Pawley et al. 1995; Ye et al. 2013; etc), isothermal compressibility (Crichton and Ross 2002; Kuribayashi et al. 2004; Freidrich et al. 2002; Holl et al. 2006; Ross and Crichton 2001), and adiabatic elastic moduli (Fritzel and Bass 1997; Jacobsen et al. 2008; Jiang et al. 2006; Sanchez-Valle et al. 2006; Sinogeikin and Bass 1999; Phan 2009; Xia et al. 1998). In this study, we examined the crystal structure of a Fe-bearing, OH-chondrodite sample by single-crystal X-ray diffraction and determined the lattice coefficients of thermal expansivity between 150 and 800 K. Brillouin spectroscopy was used to measure a set of velocities from three different platelets that constrain the thirteen independent C_{ij} of the elasticity tensor. By comparing the current results with physical properties of other DHMS phases along the forsterite-brucite join, we establish trends as a function water content that can be used to model the physical properties of mineral assemblages found in hydrated subducting slabs.

Experiments

Sample synthesis and composition

The Fe-bearing OH-chondrodite crystals were synthesized in the 5000-ton multi-anvil press at Bayerisches Geoinstitut, Bayreuth, Germany, run SZ0407B (Smyth et al. 2006). An outer 3.5-mm welded Pt capsule contained two separate 1.6 mm-diameter welded Pt inner capsules in a matrix of brucite to maintain H activity. The inner capsule contained a 1-mm single-crystal cube of San Carlos olivine, plus a mixture of brucite and forsterite. The inner capsules also contained small amount of a Re-ReO_2 oxygen buffer to maintain the iron in the ferrous state. The run was made in an 18-mm sintered MgO octahedron using 54-mm WC cubes with 8-mm corner truncations. The nominal pressure was 12 GPa at 1250ºC with a heating duration of 180 min. The original objective of the experiment was to hydrate the San Carlos olivine, but rupture of the inner capsule exposed the San Carlos olivine to excess brucite, with which it reacted to form Phase A, chondrodite, and clinohumite. The chondrodite crystals were up to 0.25 mm in diameter and light tan in color.

A single crystal about 120 μm in size was selected and polished for chemical analysis by electron microprobe following the experimental procedure described previously for the coexisting clinohumite (Ye et al. 2013). Six points at different locations of the crystal were chosen for analysis, and the average values together with their standard deviations are listed in *Table 2*. The water content was calculated to be 5.26 wt.%, assuming the molar ratio of H:O to be 2:10. The formula is expressed as $Mg_{5.047(4)}Fe_{0.058(2)}Ti_{0.0001}Mn_{0.0004(1)}Ni_{0.0018(5)}Al_{0.0017(2)}Ca_{0.0008(2)}Si_{1.945(3)}O_{10}H_2$, and Fe mol% = Fe/(Fe+Mg) = 1.1 % which is lower than those of the coexisting OH-clinohumite (4 % Fe) (Ye et al. 2013) and hydrous olivine (3 % Fe) (Jacobsen et al. 2008, hy-Fo_{97}) in the run products.

Single-crystal X-ray diffraction (XRD)

A single crystal of OH-chondrodite measuring 100 × 85 × 80 μm^3 was chosen for X-ray diffraction at ambient conditions. Unit-cell parameters were refined on a Bruker P4 four-circle diffractometer with a dual-scintillation point detector system using an 18-kW rotating Mo-anode X-ray source operating at 50 kV and 250 mA. The average wavelength for Mo$K\alpha_1$- $K\alpha_2$ mixed characteristic wavelengths was determined to be 0.71073 Å by measuring a spherical single crystal of anhydrous forsterite (Fo_{100}). Least squares fitting was performed on 48 centered reflections within the following classes: (120), $(1\,\bar{1}\,2)$, $(1\,\bar{2}\,2)$, $(1\,\bar{3}\,1)$, (130), (112), $(1\,\bar{3}\,2)$, (131), (210), $(1\,\bar{1}\,3)$, $(1\,\bar{2}\,3)$, (122), $(1\,\bar{4}\,1)$, (211), $(2\bar{1}2)$, $(2\,\bar{2}\,3)$, (222), and $(2\,\bar{4}\,1)$, and the refined unit-cell parameters at ambient condition are: a = 4.7459(2) Å, b = 10.3480(7) Å, c = 7.9002(6) Å, α = 108.702(7)°, and V = 367.50(4) $Å^3$. Intensity data were collected using a Bruker APEX II CCD detector mounted on a P4 diffractometer up to 2θ = 75°. Refinement of atomic positions and anisotropic displacement parameters was carried out using SHELXL-97 (Sheldrick 2008) in the software package WinGX (Farrugia 2012), with the default neutral atom scattering factors in SHELXL-97. In total, 10333 reflections were collected with 1915 unique and 1833 with $I > 4\sigma$ used in the refinement. Model fit parameters are: R_1 = 0.0213 for $I > 4\sigma$, and 0.0223 for all the unique reflections; goodness of fit (GooF) = 1.674; and for merging of equivalent reflections, R_{int} = 0.039.

The refined atomic position coordinates and occupancy factors are listed in *Table 3*, and the anisotropic displacement parameters are given in *Appendix 1*. In this study, Fe and Mg occupancies in the

M1, M2 and M3 sites were refined, as well as Si occupancy, and the O occupancies were fixed at full occupancy. In addition, the H position was refined with an isotropic displacement parameter (U_{eq}) fixed at 0.054.

The same single crystal of OH-chondrodite was then used for thermal expansion measurements below and above room temperature. At each temperature step, the refinement of unit-cell parameters was performed using the same experimental procedure as the room-temperature measurement described above. Low-temperature measurements were carried out at 253 K, 203 K and 153 K. Temperatures were measured and controlled by a Bruker LT-2A controller and N_2 gas stream nozzle. For high-temperature measurements, the crystal was transferred to a silica glass capillary, sealed at both ends. Ten high-temperature steps were carried out from 350 K to 787 K using a Bruker high-temperature device with a two-prong ceramic-coated Pt wire radiant heater and an Omega temperature control unit (Ye et al. 2009). The refined unit-cell parameters at low and high temperatures are given in *Appendix 2*.

Brillouin Spectroscopy

Three crystals of OH-chondrodite (from run SZ0407B) were prepared for Brillouin scattering experiments by double-sided polishing to produce parallel plates measuring about 100 µm across and 30-50 µm thick. Polishing was carried out with 3 µm diamond lapping film and finishing with 1 µm and then finally 0.5 µm diamond lapping film to produce an optical-quality surface free of visible scratches.

Prior to Brillouin spectroscopy, Raman spectroscopy was carried out on each of the three platelets. Unpolarized Raman spectra were obtained using a 200 mW Ar-ion laser (λ = 514.532 nm) with a confocal optical setup in back-scattering geometry using holographic optics and a single-grating 0.5 m spectrometer with a 1100 x 330 pixel CCD camera. Raman spectra of the three OH-chondrodite crystals used in the Brillouin scattering experiments are shown in *Fig. 3 (A-D)*.

Brillouin Spectra were obtained in a forward symmetric scattering geometry (Speziale and Duffy 2002; Speziale et al. 2014) with a six-pass Sandercock tandem Fabry-Perot interferometer, using a solid-state laser (λ = 532.15 nm, 150 mW at the sample). Acoustic velocities (V_i) were determined as:

$$V_i = \frac{\Delta\omega_i \lambda}{2\sin(\frac{\theta}{2})}\ , \qquad (1)$$

where $\Delta\omega_i$ is the Brillouin scattering frequency shift of the acoustic modes, and θ is the scattering angle in the sample (70° in this study). For each platelet, measurements were performed in ~5-10° steps with the total number of spectra in a given platelet depending on its size and the quality of the signal. Measured acoustic velocities are plotted as functions of azimuthal angle in *Fig. 4 (A-C)*. Further details about the Brillouin scattering measurements can be found in Speziale and Duffy (2002) and Speziale et al. (2014).

Three platelets were used for Brillouin scattering, with the orientation of each platelet defined with three Eulerian angles (θ, ϕ, χ). Chondrodite has a monoclinic structure with thirteen elastic constants: C_{11}, C_{22}, C_{33}, C_{44}, C_{55}, C_{66}, C_{12}, C_{13}, C_{23}, C_{15}, C_{25}, C_{35}, and C_{46}. The elastic constants and acoustic velocities are related by Christoffel's equation (Every 1980):

$$\det | C_{ijkl} n_j n_l - \rho V_{P,S}{}^2 \delta_{ik} | = 0 \qquad (2)$$

where C_{ijkl} is the elastic tensor in full suffix notation, n_i is the direction cosine of the phonon propagation direction, density ρ = 3.099 g/cm^3 (according to the composition determined by EPMA and unit-cell volume from single-crystal XRD at ambient condition), and $V_{P,S}$ is the acoustic velocity of either longitudinal (V_P) or transverse (V_S) in the Brillouin spectra. The inversion was carried out by non-linear lest-squares using Levenberg-Marquardt method (Press et al. 1988) with closed-form expressions for the Christoffel equation given by Every (1980). The inversion process was iterative. The elastic constants of Sinogeikin and Bass (1999) were used as the initial model and held fixed while the inversion was performed for the three Eulerian angles defining the orientation of each plane. The relationship between the Eulerian angles and the direction cosines of the phonon propagation direction is given by Shimizu (1995). In subsequent inversions, the elastic constants and orientations were alternately varied or allowed to vary together, and the process was continued until convergence was achieved. Different sets of initial elastic constants were tested to confirm that the final results were insensitive to the starting model. The results are shown in *Fig. 4(A-C)*. The good quality of the fit is demonstrated by the small root-mean-square difference between the measured and calculated velocities which was V_{RMS} = 39 m/s.

Results and Discussion

Raman spectroscopy

Unpolarized Raman spectra of the three OH-chondrodite platelets used for Brillouin scattering are shown in *Fig. 3*. The spectra are generally similar to previous Raman studies of OH-chondrodite (Lin et al. 1999; Mernagh et al. 1999). In *Fig. 3*, the polished plane orientation is expressed as (*hkl*), fitted from the velocity dispersion curves in the Brillouin scattering study. Band assignments for some of the modes shown in *Fig. 3* are given elsewhere (Cynn et al. 1996; Lin et al. 1999). In the O-H stretching region, we find a similar strong doublet as was found for F-free synthetic OH-chondrodite (Lin et al. 1999). The main band positions shown in *Fig. 3* are 3525 and 3565 cm^{-1}, which are shifted by about 10 cm^{-1} from the positions shown by Lin et al. (1999) at 3515 and 3554 cm^{-1}. Also in *Fig. 3* is shown a deconvolution of the O-H stretching doublet (dashed lines), which is composed of at least four separate bands at 3525, 3560, 3565, and 3580 cm^{-1}. The 3525 cm^{-1} band may be further deconvolved into three separate bands to best fit the observed spectrum.

Crystal Structure

According to the refined Mg and Fe occupancies in *Table 3*, the total Fe mol% is 0.9(4)%, consistent within uncertainty with that of (1.1 mol%) obtained from electron microprobe analyses. The Fe content from single-crystal XRD (site occupancy) is an approximation as minor elements (Ti, Ni, Mn, Ca, Al, < 0.04 mol%) were ignored in the structural refinement. The Si occupancy refinement from X-ray diffraction is consistent with that from microprobe analyses. The bond lengths and polyhedral volumes were calculated using the software package XTALDRAW (Downs et al. 1993), and listed in *Table 4*. The octahedral volumes shows the order of M2 > M3> M1, and the Si tetrahedral volume is 2.21(1) $Å^3$. The hydrogen bond geometry shows an O5-H distance of 1.06(2) Å and O5…H of 2.12(2) Å with a hydrogen bond angle of 122.7˚. The O5-H bond length (O/F-H bonds in some chondrodites) has been refined by neutron diffraction (Friedrich et al. 2001 and Kunz et al. 2006), as well as X-ray diffraction (Ottolini et al. 2000 and Friedrich et al. 2002). Neutron diffraction better reflects the OF5-H interatomic distances than single-crystal X-ray diffraction. Friedrich et al. (2001) reported a bond length of 1.029(6) Å for OF-H and 1.872(6) Å for OF5…H, while Kunz et al. (2006) reported 0.976(7) Å and 1.940(7) Å, respectively. Our O5-H bond length is close to those from neutron experiments, whereas the O5…H interatomic distance is 10 % longer than previous results from neutron diffraction.

To compare the compositional effects of Fe, F, and Ti on the crystal structure of chondrodite, the unit-cell volumes and M-OF bond lengths are summarized in *Table 5* for this study (SZ0407B) and literature values with the following abbreviations used throughout: Berry and James 2002, B02; Friedrich et al. 2001 and 2002, F01 and F02; Fujino and Takéuchi 1978, F78; Gibbs et al. 1970, G70; Kuribayashi et al. 2004, K04; Kunz et al. 2006, K06; Ottolini et al. 2000, O00; Yamamoto 1977, Y77. The α angle in Sample F78 is significantly larger than other samples in *Table 5*, which is likely due to the effect of Ti^{4+} incorporation (Robinson et al. 1973). In addition, α angle values in SZ0407B and Y77 are 0.35~0.4° smaller than those in Y77, B02, G70, O00, F01, F02, K06 and K04, implying that F^- might increase the angle. The unit cell volumes decrease in the order of SZ0407B and Y77 > F78 > F01, F02, K06 and K04 > B02 and G70 > Y77 consistent with the order of decreasing ionic radii ($Fe^{2+} > Mg^{2+} > Ti^{4+}$) and anions ($O^{2-} > F^-$). Samples SZ0407B, Y77 and F78 are F-free, while F78 has a high Ti^{4+} concentration of 8.4 mol%. Samples F01, F02, K06 and K04 have higher Fe^{2+} concentrations than B02, G70 and Y77, and B02 has the highest F^- content among these samples. The most significant effect of F^- on the crystal structure is that F^- decreases distances between OFOH and surrounding cations, i.e. one M2-OF bond and two M3-OFOH bonds. Samples SZ0407B and Y77 typically have larger M-OF bond lengths than other samples, as shown in *Table 5*, while sample F78 has significantly smaller M3-OF bond lengths, due to the occupancies of smaller cations Ti^{4+} in M3 site. Fe^{2+} should increase the M-O bond lengths but such effect is not well observed here, perhaps because of the low concentration of Fe^{2+} in the reported crystal structures and, possible technical discrepancies among different measurements.

Thermal Expansivity

To relate the anisotropy of thermal expansion to the crystal structure, the principal axes of thermal expansion are determined for this monoclinic structure, reducing the number of thermal expansion coefficients from 4 to 3: X_1, X_2, and X_3 (Cliffe and Goodwin 2012). The variations with temperature of the principle expansion axes are listed in *Appendix 2*, and the average axial thermal expansion coefficients are listed in *Table 6*, as well as the orientations of the principle expansion axes. There is no difference between *a* and X_1 for a-unique monoclinic structure, while the thermal expansion coefficient of X_2 is 8% smaller than that of *b* axis for the compensation of α angle (>90˚) expansion.

The thermal expansion coefficient is defined as:

$$\alpha(T) = \frac{1}{V}\left(\frac{\partial V}{\partial T}\right)_P = \left(\frac{\partial \ln(V)}{\partial T}\right)_P . \quad (3)$$

Fei (1995) proposed a useful formula for modeling $\alpha(T)$ above room temperature:

$$\alpha(T) = a_0 + a_1 T + \frac{a_2}{T^2} . \quad \text{(Fei equation)} \quad (4)$$

On the basis of the Mie-Grüneisen-Debye Equation of Stae, Suzuki (1975), Suzuki et al. (1979) and Kumar (1995, 1996, 2000) developed expression for the unit-cell volume as function of temperature:

$$V_0(T) = V_0(0)\cdot[1 + \frac{1-(1-4k\cdot E_{th}(T)/Q_0)^{1/2}}{2k}] \quad \text{(Suzuki equation)} \quad (5)$$

$$V_0(T) = V_0(0)\cdot[1 - \frac{\ln[1-(2k+2)\cdot E_{th}(T)/Q_0]^{1/2}}{2k+2}] \quad \text{(Kumar equation)} \quad (6)$$

where k = (K_T'-1)/2 = 2.25 (K_T' = 5.5 as in Table 1), Q_0 = $V_0(0)K_{T0}(0)/\gamma_{MGD}$. $V_0(0)$ and $K_{T0}(0)$ are the volume and isothermal bulk modulus taken at 0 K and 0 GPa. γ_{MGD} is a parameter related to the thermodynamic Grüneisen parameter γ_{th} (Barron et al. 1980). The thermal energy $E_{th}(T)$ is expressed by the Debye model:

$$E_{th}(T) = \frac{9nRT}{(\Theta_D/T)^3}\int_0^{\Theta_D/T}\frac{x^3}{e^x-1}\cdot dx \quad (7)$$

where R is the gas constant, n is the number of atoms in the formula unit (19 for OH-chondrodite), and Θ_D is the Debye temperature, and the acoustic Debye temperature Θ_{ac} is given by:

$$\Theta_{ac} = \frac{h}{k}\cdot(\frac{3N}{4\pi})^{1/3}\cdot(\frac{n\cdot\rho}{M})^{1/3}\cdot v_m \quad (8)$$

$$\frac{3}{v_m^3} = \frac{2}{v_s^3} + \frac{1}{v_p^3} \quad (9)$$

where h, k, N are Boltzmann, Plank and Avagadro's constants, respectively, and M is the molar mass. The calculated Θ_{ac} values for phase A, chondrodite and clinohumite are listed in *Table 1*. The Θ_{ac} values for

247 these DHMS phases are close to that (729 K) for San Carlos olivine (Liu and Li 2006), and we adopt Θ_D =
248 741 K to calculate the thermal expansion coefficient of chondrodite in this study.

249 The unit-cell volume and principal expansion axes are plotted in *Fig. 5(A)* as a function of
250 temperature, and fitted by the curves calculated from Fei equation (Eq. 4). The principal expansion axes
251 show an order of $\alpha_{X3} > \alpha_{X1} > \alpha_{X2}$. We derive the thermal expansion coefficients for unit-cell volume as: a_0
252 = 40.9(7) × 10^{-6} K^{-1}, a_1 = 2.8(5) × 10^{-9} K^{-2}, a_2 = -0.81(3) K according to Fei equation. Next, the $V(T)$ dataset
253 from this study is also fitted by Suzuki and Kumar equations (Eq. 5 and 6). We used K_{T0}(298K) = 114 GPa
254 (Table 1), and assuming that OH-chondrodite has the same dK_{T0}/dT as forsterite (-0.023 GPa/K, Kroll et al.
255 2012), we obtain K_{T0}(0K) = 121 GPa. Then the fittings result in γ_{MGD} = 1.19(6) from Kumar equation;
256 1.21(8) from Suzuki equation; and V_0(0K) = 365.8(3) $Å^3$ for both Kumar and Suzuki equations.

257 The calculated $\alpha_V(T)$, calculated from Fei, Kumar and Suzuki equations, are plotted in *Fig. 5(B)*,
258 respectively, and extrapolated to 1500 K where the breakdown of OH-chondrodite was observed (Burnley
259 and Navrotsky 1996). The Fei equation generates negative α_V below 140 K, whereas the Kumar and Suzuki
260 equations give larger and more reasonable α_V at such low temperatures. From 200 K to 800 K, these three
261 equations agree with each other well, with discrepancy of 5% at 800 K. When extrapolated to 1500 K, the
262 Kumar and Suzuki equations indicate α_V values 20% and 13 % larger, respectively, compared with that
263 from Fei equation. In addition, for $\alpha(T)$ relation as proposed by Fei (1995), the sum of the thermal
264 expansion coefficients for principal axes at the measured temperatures is also plotted in Fig. 5(B), which
265 consistent with the solid curve of $\alpha_V(T)$ from Fei equation.

266 The axial thermal expansivity for the present Fe-bearing OH-chondrodite sample shows anisotropy
267 in the order of $\alpha_c > \alpha_a > \alpha_b$, whereas axial compressibilities determined from single-crystal XRD data at
268 high pressure yield an anisotropy of $\beta_b \approx \beta_c > \beta_a$ for Fe-free OH-chondrodite (Ross and Crichton 2001;
269 Kuribayashi et al. 2004), and $\beta_b > \beta_c > \beta_a$ for Fe,F-bearing samples (Friedrich et al. 2002; Kuribayashi et al.
270 2004). The axial compressibilities are also consistent with the elasticity studies: $C_{11} > C_{33} \approx C_{22}$ for Fe-free
271 OH-chondrodite (this study, in the following discussion), and $C_{11} > C_{33} > C_{22}$ for Fe,F-bearing sample
272 (Sinogeikin and Bass 1999). Here, the elastic moduli are transferred to *a*-unique monoclinic symmetry to
273 be consistent with the studies of crystal structure and isothermal compression. In this study, we find that the

274 α angle increases with temperature, which is consistent with the observations that α decreases with
275 pressure (Ross and Crichton 2001; Friedrich et al. 2002; Kuribayashi et al. 2004). The angle α increases as
276 temperature increasing with a thermal expansion coefficient of 1.43(10) x10^{-6} K, consistent with that for
277 clinohumite (1.41~1.53 x10^{-6} K from Ye et al. 2013).

278 The average volume thermal expansion coefficients (α_0) for the DHMS phases along the forsterite-
279 brucite join are plotted in *Fig. 6*, as a function of water content (C_{H2O}, expressed as wt.% H_2O). The $\alpha_0(V)$
280 values are recalculated over temperature range of 300 - 787 K for forsterite (Ye et al. 2009), clinohumite
281 (Ye et al. 2013) and chondrodite (this study) to allow for consistent comparison with previous experiments
282 on phase A (Pawley et al. 1995) and brucite (Fukui et al. 2003). There have been many previous studies on
283 thermal expansivity of anhydrous forsterite (e.g. Ye et al. 2009; Kroll et al. 2012; and Trots et al. 2012). To
284 simplify *Fig. 6*, we plotted the anhydrous forsterite thermal expansivity data from Ye et al. (2009) as
285 representative. The α_0 for hydrous forsterite (0.89 wt% H_2O) is ~ 0.8×10^{-6} K^{-1} larger than that for
286 anhydrous forsterite. The Fe-bearing clinohumite (Fe % = 4.1 mol%) shows α_0 ~ 2.2×10^{-6} K^{-1} smaller than
287 Fe-free clinohumite (Ye et al. 2013). The α_0 for the current OH-chondrodite sample is 40.8(4) $\times10^{-6}$ K^{-1} in
288 the range of 300 – 787 K, whereas it is 38.0(9) $\times10^{-6}$ K^{-1} in 153 – 787 K.

289 A linear regression for the data of *Fig. 6* yields a systematic relation between α_0 and C_{H2O} as:

290 $$\alpha_0\ (10^{-6}\ K^{-1}) = 35.3(4) + 1.02(3) \times C_{H2O}\ (wt\%) \qquad (R^2 = 0.9947) \qquad (10)$$

291 Each additional 1 wt% H_2O content increases α_0 by 1.02(3)$\times10^{-6}$ K^{-1} (or about 3 %). Thus, the thermal
292 expansion coefficient increases with H_2O content for DHMS along the forsterite-brucite join, which is
293 consistent with the observation that the bulk moduli decrease as H_2O content increases (Ross and Crichton
294 2001; Holl et al. 2006; Jacobsen et al. 2008; Sanchez-Valle et al. 2006).

295 After heating to 787 K, the single crystal of OH-chondrodite was quenched to room temperature,
296 and the unit cell parameters after heating are: a = 4.7455(4) Å, b = 10.3475(8) Å, c = 7.9008(9) Å, α =
297 108.706(8)°, and V = 367.47(7) $Å^3$, consistent with the initial ones before heating. We conclude that this
298 Fe-bearing OH-chondrodite sample persisted to 787 K at ambient pressure without any observable phase
299 transition or dehydration.
300

Elastic moduli

The calculated elastic moduli for OH-chondrodite (Fe/(Mg+Fe) = 1.1 %) are listed in *Table 7*, with comparison to F-bearing chondrodite (Fe/(Mg+Fe) = 5.5 %, F/(F+OH) = 32%, Sinogeikin and Bass 1999). Nearly all of the longitudinal and shear elastic constants are lower than those reported by Sinogeikin and Bass (1999) for a F-rich natural chondrodite. The Brillouin inversion was performed in standard monoclinic symmetry (*b*-unique, $P2_1/c$) where zigzag chains of edge-sharing octahedra are aligned along the *a* axis and lie in the plane perpendicular to the *b* axis. The elastic indices are also reported in the *a*-unique coordinate system ($P2_1/b$) (values given in parentheses in *Table 7)* to facilitate comparison with the studies of the crystal structure. The longitudinal constants C_{22} and C_{33} (in standard monoclinic symmetry hereafter) are close to the values from Sinogeikin and Bass (1999), whereas C_{11} is 12% smaller. The shear constants C_{55} and C_{66} are about 5 % smaller, while C_{44} is 8% smaller. The off-diagonal moduli are not constrained as well in either study. The Voigt / Reuss bounds, and Voigt-Reuss-Hill (VRH) average of the aggregate moduli (Watt 1980) for OH-chondrodite are summarized in *Table 8*. The bulk modulus found here is identical within uncertainty to that obtained by Sinogeikin and Bass (1999), and consistent with those reported in static compression studies (Ross and Crichton, 2001, Kuribayashi et al., 2004; Friedrich et al., 2002). The shear modulus, G_0, is however about 6% lower than that reported by Sinogeikin and Bass (1999) for a natural F-bearing sample, indicating that the shear modulus may increase with F content.

Using the density (ρ), isothermal bulk modulus (K_{S0}), thermal expansion coefficient (α_0) and heat capacity (C_P) listed in *Table 1*, we calculated the Grüneisen parameter (γ) for phase A, OH-chondrodite and OH-clinohumite, from the formula:

$$\gamma = \frac{\alpha \cdot K_S}{\rho \cdot C_P} \qquad (11)$$

The calculated γ values are also listed in *Table 1*. The Grüneisen parameter for phase A (1.69(8)), chondrodite (1.66(4)), and clinohumite (1.50(4)) is larger than that for forsterite (1.28, Gillet 1991), since phase A, chondrodite and clinohumite have smaller C_P and ρ values than forsterite, whereas variation in the product $\alpha \cdot K_S$ is relatively less significant among these phases.

Because the Reuss bound on the bulk modulus, $K_{S0,}$ corresponds to constant stress across grain boundaries, which is relevant for static compression studies, we calculate the isothermal Reuss bound bulk modulus for OH-chondrodite: K_{T0} = 114.2(14) GPa, with K_{S0} = 116.4(12) GPa and the formula:

$$K_T = \frac{K_S}{1+\alpha\cdot\gamma\cdot T} \quad (12)$$

Next, on the basis of reported compression datasets for Fe-free OH-chondrodite (Ross and Crichton 2001; Kuribayashi et al. 2004), we refined the pressure derivative of the bulk modulus, K_T', and obtain K_T' = 5.5(1) (*Fig. 7*) by fixing K_{T0} at 114.2 GPa, the Reuss bound from Brillouin scattering. *Fig. 7* also shows that both these high-pressure datasets are consistent with each other. It should be noted that our OH-chondrodite has 1.1 mol% Fe, but such a low Fe concentration should probably be expected to have little effect on the bulk modulus. The refined results are also included in *Table 8*. Our results are consistent with the chondrodite sample from Friedrich et al. (2002) (Fe-free, F/(F+OH) = 0.32) which further indicates that F content does not strongly affect the bulk modulus. It should also be noted that the study by Faust and Knittle (1994) could be affected by non-hydrostatic stress for compression to 42 GPa in the pressure medium of methanol, ethanol and water mixture.

Over the past three decades, extensive studies have been carried out on the elasticity of DHMS phases along the forsterite-brucite join (Suzuki et al. 1983; Webb 1989; Zha et al. 1996 and 1998; Fritzel and Bass 1997; Sinogeikin and Bass 1999; Sanchez-Valle et al. 2006; Jacobsen 2008 and 2009; Phan 2009; as well as this study). The density (ρ), elastic moduli (K_{S0} and G_0,Voigt-Reuss-Hill averages) and acoustic velocities (V_P and V_S) are summarized in *Fig. 8(A)*, *(B)* and *(C)*, respectively, with linear regression fittings listed below:

$$\rho\ (\mathrm{g/cm^3}) = 3.27(2) - 0.029(2)\times C_{H2O} \quad (R^2 = 0.9767) \quad (13)$$

$$K_{S0}\ (\mathrm{GPa}) = 129.6(9) - 2.69(8)\times C_{H2O} \quad (R^2 = 0.9898) \quad (14)$$

$$G_0\ (\mathrm{GPa}) = 79.3(6) - 1.45(5)\times C_{H2O} \quad (R^2 = 0.9866) \quad (15)$$

$$V_P\ (\mathrm{km/s}) = 8.54(4) - 0.073(3)\times C_{H2O} \quad (R^2 = 0.9724) \quad (16)$$

$$V_S\ (\mathrm{km/s}) = 4.95(3) - 0.036(2)\times C_{H2O} \quad (R^2 = 0.9565) \quad (17)$$

The liner fits show that 1 wt% H_2O reduces K_{S0} and G_0 by 2.69(8) GPa (2%) and 1.45(5) GPa (2%), respectively, We also find that the isothermal bulk modulus (K_{T0}) decreases by 2.71 GPa for every 1 wt%

H_2O added along the forsterite-brucite join (Ross and Crichton 2001; Holl et al. 2006). On the other hand, a linear relation for density versus water content is plotted in *Fig. 8(A)*. Addition of 1wt% H_2O reduces ρ by 0.029(2) g/cm^3, and linear regressions for moduli and velocities versus density (Birch's law) could be fulfilled on basis of Eq. (13).

In summary, we have presented new thermoelastic properties of OH-chondrodite, which was synthesized at 12 GPa and 1523 K, and coexists with OH-clinohumite and hydrous olivine. The synthesis conditions correspond to the pressure-temperature condition around 360-km depth in a hydrous subducting slab. The chondrodite sample was characterized by multiple experimental methods: electron microbe, Raman spectroscopy, single-crystal X-ray diffraction (153–787 K), and finally by Brillouin spectroscopy. For DHMS phases along the forsterite-brucite joint, every 1 wt% increase in C_{H2O} increases the mean thermal expansion coefficient (α_0) by 3 %, decreases the moduli (K_{T0}, K_{S0} and G_0) by 2 %, and decreases the seismic velocities (V_P and V_S) by ~ 8 %. Hydration also enlarges the Grüneisen parameters for phase A, chondrodite and clinohumite by 17~32 %, compared with anhydrous forsterite. The elastic properties OH-chondrodite found in this study are consistent with the previous isothermal compression studies of Fe,F-free samples. The thermal expansion coefficient $\alpha(T)$ at ambient pressure is constrained by different models. The Fei equation yields: $\alpha_V = 2.8(5)\times10^{-9}(K^{-2})\times T + 40.9(7)\times10^{-6}(K^{-1}) - 0.81(3)(K)/T^2$ (150—800 K); Suzuki and Kumar equations fit: V_0(0 K) = 365.8(3) Å^3, Θ = 741 K, γ_{MGD} = 1.20(9) (γ = 1.66(4) calculated from Eq. 11). The thermoelastic properties reported in this study are important to anchoring more complete *P-V-T* equations of state for chondrodite and other DHMS phases in future studies at simultaneous high pressure and high temperature.

Acknowledgements

This work was supported by US NSF grants EAR-1452344 (SDJ), EAR-1113369 (JRS), and EAR-114854 (TSD). SDJ also acknowledges support from the Carnegie/DOE Alliance Center (CDAC), and the David and Lucile Packard Foundation. Synthesis was performed at Bayerisches Geoinstitut, University of Bayreuth, Germany, and supported in part by the Alexander von Humboldt Foundation.

References:

Angel, R.J., Frost, D.J., Ross, N.L., and Hemley, R.J. (2001) Stabilities and equations of state of dense hydrous magnesium silicates. Phys Earth Planet Inter, 127, 181-196.

Barron, T.H.K., Collins, J.G., and White, G.K. (1980) Thermal expansion of solids at low temperatures. Adv. Phys., 29, 609-730.

Berry, A.J. and James, M. (2001) Refinement of hydrogen positions in synthetic hydroxyl-clinohumite by powder neutron diffraction. Am Mineral, 86: 181-184.

Berry, A.J. and James, M. (2006) Refinement of hydrogen positions in natural chondrodite by powder neutron diffraction: Implications for the stability of humite minerals. Miner Mag, 66: 441-449.

Burnley, P.C. and Navrotsky, A. (1996) Synthesis of high-pressure hydrous magnesium silicates: Observations and analysis. Am Mineral 81: 317-326.

Cliffe, M.J. and Goodwin, A.L. (2012) PASCal: A principal-axis strain calculator for thermal expansion and compressibility for thermal expansion and compressibility determination. J Appl Crystallogr, 45, 1321-1329.

Crichton, W.A. and Ross N.L. (2002) Equation of state of dense hydrous magnesium silicate Phase A, $Mg_7Si_2O_8(OH)_6$. Am Mineral, 87: 333-338.

Cynn, H., Hofmeister, A.M., Burney, P.C., and Navrotsky, A. (1996) Thermodynamic properties and hydrogen speciation from vibrational spectra of dense hydrous magnesium silicates. Phys Chem Miner, 23: 361-376.

Downs, R.T., Bartelmehs, K.L., Gibbs, G.V., and Boisen M.B. (1993) Interactive software for calculating and displaying X-ray or neutron powder diffractometer patterns of crystalline materials. Am Mineral, 78: 1104-1107.

Engi M. and Lindsley, D.H. (1980) Stability of titanian clinohumite: experiments and thermodynamic analysis. Contrib Mineral Petrol, 72, 1935-1938.

Evans, B.W. and Trommsdorff, V. (1983) Fluorine hydroxyl titanian clinohumite in alpine recrystallized garnet peridotite: Compositional controls and petrologic significance. Am J Sci, 283, 355-369.

Every, A.G. (1980) General closed-form expressions for acoustic waves in elastically anisotropic solids. Phys Rev, B22: 1746-1760.

409 Faust, J. and Knittle, E. (1994) Static compression of chondrodite: Implications for water in the upper
410 mantle. Geophys Res Lett, 21, No 18: 1935-1938.
411 Farrugia, L.J. (2012) WinGX and ORTEP for Windows:an update. J. Appl. Cryst., 45, 849-854.
412 Fei, Y. (1995) Thermal expansion. In "Mineral Physics & Crystallography", Ahrens, J. T. (in ed.) AGU
413 Ref. Shelf, 2, 29-44.
414 Friedrich A., Lager, G.A., Kunz, M., Chakoumakos, B.C., Smyth, J.R., and Schultz, A.J. (2001)
415 Temperature-dependent single-crystal neutron diffraction study of natural chondrodite and
416 clinohumite. Am Mineral, 86: 981-989.
417 Friedrich, A., Lager, G.A., Ulmer P., Kunz, M., and Marshall, W.G. (2002) High-pressure single-crystal X-
418 ray and powder neutron study of F,OH/OD-chondrodite: Compressibility, structure, and hydrogen
419 bonding. Am Mineral, 87: 931-939.
420 Fritzel, T.L.B. and Bass, J.D. (1997) Sound velocities of clinohumite, and implications for water in Earth's
421 upper mantle. Geophys Res Lett, 24(9): 1023-1026.
422 Fujino K. and Takéuchi, Y. (1978) Crystal chemistry of titanian chondrodite and titanian clinohumite of
423 high-pressure origin. Am Mineral, 63: 535-543.
424 Fukui T., Ohtaka, O., Suziki T., and Funakoshi, K. (2003) Thermal expansion of $Mg(OH)_2$ brucite under
425 high pressure and pressure dependence of entropy. Phys Chem Miner, 30: 511-516.
426 Gibbs, G.V., Ribbe, P.H., and Anderson, C.P. (1970) The crystal structure of the humite minerals. II.
427 Chondrodite. Am Mineral, 55: 1182-1194.
428 Gillet, P. (1991) High-temperature thermodynamic properties of forsterite. J Geophys Res, 96, B7: 11805-
429 11816.
430 Holl, C.M., Smyth, J.R., Manghnani, M.H., Amulele, G.M., Sekar, M., Frost, D.J., Prakapenka, V.B., and
431 Shen, G. (2006) Crystal structure and compression of an iron-bearing Phase A to 33 GPa. Phys
432 Chem Miner, 33: 192-199.
433 Holland, T.J.B. and Powell R. (1998) An internally consistent thermodynamic data set for phases of
434 petrological interest. J Metamorphic Geol, 16: 309-343.
435 Irifune, T., Kubo, N., Isshiki, M., and Yamasaki, Y. (1998) Phase transformations in serpentine and
436 transportation of water into the lower mantle. Geophys Res Lett, 25, No 2, 203-206.

Jacobsen, S.D., Jiang, F., Mao Z., Duffy, T.S., Smyth, J.R., Holl, C.M., and Frost, D.J. (2008) Effects of hydration on the elastic properties of olivine. Geophys Res Lett, 35: L14303.

Jacobsen, S.D., Jiang, F., Mao Z., Duffy, T.S., Smyth, J.R., Holl, C.M., and Frost, D.J. (2009) Correction to "Effects of hydration on the elastic properties of olivine". Geophys Res Lett, 36: L12302.

Jiang, F., Speziale, S., and Duffy, T.S. (2006) Single-crystal elasticity of brucite, $Mg(OH)_2$, to 15 GPa by Brillouin scattering. Am Mineral, 91: 1893-1900.

Kanzaki, M. (1991) Stability of hydrous magnesium silicate in the mantle transition zone. Phys Earth Planet Inter, 66: 307-312.

Kawamoto, T. (2006) Hydrous phases and water transport in the subducting Slab. Rewiews Mineral Geochem, 62, 273-289.

Khodyrev, O.Y., Agoshkow, V.M., and Slutsky, A.B. (1992) The system peridotite-aqueous fluid at upper mantle parameters. Trans Dokl USSR Acad Sci: Earth Sci Sect 312, 255-258.

Komabayashi, T. and Omori, S. (2006) Internally consistent thermodynamic data set for dense hydrous magnesium silicates up to 35 GPa, 1600 °C: Implications for water circulation in the Earth's deep mantle. Phys Earth Planet Inter, 156, 89-107.

Kroll, H., Kirfel, A., Heinemann, R., and Barbier, B. (2012) Volume thermal expansion and related thermophysical parameters in the Mg,Fe olivine solid-solution series. Eur J Mineral, 24: 935-956.

Kumar, M. (1995) High pressure equation of state for solids. Physica B, 212, 391-394.

Kumar, M. (1996) Application of high pressure equation of state for different classes of solids. Physica B, 217, 143-148.

Kumar, M. (2003) Thermoelastic properties of minerals. Phys Chem Minerals, 30, 556-558.

Kunz, M., Lager, G.A., Burgi, H.B., and Fernandez-Diaz, M.T. (2006) High-temperature single-crystal neutron diffraction study of natural chondrodite. Phys Chem Miner, 33: 17-27.

Kuribayashi, T., Kagi, H., Tanaka, M., Akizuki, M., and Kudoh, Y. (2004) High-pressure single crystal X-ray diffraction and FT-IR observation of natural chondrodite and synthetic OH-chondrodite. J Miner Petrol Sci, 99: 118-129.

Kuribayashi, T., Tanaka, M., and Kudoh, Y. (2008) Synchrotron X-ray analysis of norbergite,

$Mg_{2.98}Fe_{0.01}Ti_{0.02}Si_{0.99}O_4(OH_{0.31}F_{1.69})$ structure at high pressure up to 8.2 GPa. Phys Chem Miner, 35: 559-568.

Lin, C.-C., Liu, L.-G. and Irifune, T. (1999) High-pressure Raman spectroscopic study of chondrodite. Phys Chem Miner, 26, 3, 226-233.

Liu W. and Li B. (2006) Thermal equation of state of $(Mg_{0.9}Fe_{0.1})_2SiO_4$ olivine. Phys Earth Planet Inter, 157, 188-195.

McDonough W.F. and Sun S.-S. (1995) The composition of the Earth. Chem Geol, 120, 223-259.

McGetchin, T.R., Silver, L.T., and Chodos, A.A. (1970) Titanoclinohumite: A possible mineralogical site for water in the upper mantle. J Geophys Res, 75: 255-259.

Mernagh, T.P., Liu, L.-G., and Lin, C.-C. (1999) Raman spectra of chondrodite at various temperatures. J Raman Spect, 30, 963-969.

Ohtani, E., Mizobata, H., and Yurimoto, H. (2000) Stability of dense hydrous magnesium silicate phases in the systems Mg_2SiO_4-H_2O and $MgSiO_3$-H_2O at pressures up to 27 GPa. Phys Chem Miner, 27, 533-544.

Ottolini, L., Cámara, F., and Bigi, S. (2000) An investigation of matrix effects in the analysis of fluorine in humite-group minerals by EMPA, SIMS, and SREF. Am Mineral, 85: 89-102.

Pawley A.R., Redfern, S.A.T., and Wood B.J. (1995) Thermal expansivities and compressibilites of hydrous phases in the system MgO-SiO_2-H_2O: talc, phase A and 10-Å phase. Contrib Mineral Petrol, 122: 301-307.

Phan, H.T. (2009) Elastic properties of hydrous phases in the deep mantle: High-pressure ultrasonic wave velocity measurements on clinohumite and Phase A (dissertation). ETH Zürich, No: 18091, p125.

Press, W.H., Flannery, B.P., Teukolsky, S.A., and Vetterling, W.T. (1988) Numerical Recipes in C: The Art of Scientific Computing. Cambridge University Press.

Robinson, K., Gibbs, G.V., and Ribbe, P.H. (1973) The crystal structure of the humite minerals IV. Clinohumite and titanoclinohumite. Am Mineral, 58: 43-49.

Ross, N.L. and Crichton W.A. (2001) Compression of synthetic hydroxylclinohumite $[Mg_9Si_4O_{16}(OH)_2]$ and hydroxylchondrodite $[Mg_5Si_2O_8(OH)_2]$. Am Mineral, 86: 990-996.

Sanchez-Valle, C., Sinogeikin, S.V., Smyth, J.R., and Bass, J.D. (2006) Single-crystal elastic properties of

492 dense hydrous magnesium silicate phase A. Am Mineral, 91: 961-964.
493 Sheldrick, G.M. (2008) A short history of SHELX. Acta Cryst. A. 64, 112-122.
494 Shen, T., Hermann, J., Zhang, L, Padron-Navarta, J.A., and Chen, J. (2014) FTIR spectroscopy of Ti-
495 chondrodite, Ti-clinohumite, and olivine in deeply subducted serpentinites and implications for the
496 deep water cycle. Contrib Mineral Petrol, 167, DOI: 10.1007/s00410-014-0992-8.
497 Shieh, S.R., Mao, H.-K., Hemley, R.J., and Ming, L.C. (2000) In situ X-ray diffraction studies of dense
498 hydrous magnesium silicates at mantle conditions. Earth Planet Sci Lett, 177, 69-80.
499 Shimizu, H., 1995. High-pressure Brillouin scattering of molecular single-crystals grown in a diamond-
500 anvil cell. 1-17, In: Senoo, M., Suito, K., Kobayashi, T., Kubota, H. (eds.), High Press Res Solid.
501 Elsevier, Netherlands.
502 Sinogeikin, S.V. and Bass, J.D. (1999) Single-crystal elastic properties of chondrodite: implications for
503 water in the upper mantle. Phys Chem Miner, 26: 297-303.
504 Smyth, J.R., Frost, D.J., Nestola, F., Holl, C.M., and Bromiley, C. (2006) Olivine hydration in the deep
505 upper mantle: effects of temperature and silica activity. Geophys Res Lett 33: L15301.
506 Speziale, S. and Duffy, T.S. (2002) Single-crystal elastic constants of fluorite (CaF_2) to 9.3 GPa. Phys
507 Chem Miner, 29, 465-472.
508 Speziale, S., H. Marquardt, and T. S. Duffy (2014), Brillouin Scattering and its Application in Geosciences,
509 in *Spectroscopic Methods in Mineralology and Materials Sciences*, 78, 543-603, In: Henderson,
510 G.S., Neuville, D.R. and R. T. Downs, R.T. (eds.)Mineralogical Soc Amer, Chantilly VA.
511 Suzuki, I. (1975) Thermal expansion of periclase and olivine, and their anharmonic properties, J Phys
512 Earth, 23, 145-149.
513 Suzuki, I., Oajima, S., Seya, K. (1979) Thermal expansion of single-crystal maganosite.. J Phys Earth, 27,
514 63-69.
515 Suzuki, I., Anderson, O.L., and Sumino, Y. (1983) Elastic properties of a single-crystal forsterite Mg_2SiO_4,
516 up to 1200 K. Phys Chem Miner, 10: 38-46.
517 Taskaev, V.I. and Ilupin, I.P. (1990) Association of clinohumite and K-richterite in the kimberlite of
518 Kollektivnaya pipe. Doklady Akademii Natsional'naya USSR 310(3), 683-686.
519 Trots, D.M., Kurnosov, A., Boffa Ballaran, T., and Frost, D.J. (2012) High-temperature structural

behaviors of anhydrous wadsleyite and forsterite. Am Mineral, 97: 1582-1590.

Watt J.P. (1980) HashinShtrikman bounds on the effective elastic moduli of polycrystals with monoclinic Symmetry. J. Appl. Phys., 51, doi: 10.1063/1.327803.

Webb, S.L. (1989) The elasticity of the upper mantle orthosilicates olivine and garnet to 3 GPa. Phys Chem Miner, 16: 684-692.

Wunder, B. (1998) Equilibrium experiments in the system MgO-SiO_2-H_2O (MSH): stability fields of clinohumite-OH [$Mg_9Si_4O_{16}(OH)_2$], chondrodite-OH [$Mg_5Si_2O_8(OH)_2$] and phase A [$Mg_7Si_2O_8(OH)_6$]. Contrib Mineral Petrol, 132: 111-120.

Wunder, B., Medenbach, O., Daniels, P., and Schreyer, W. (1995) First synthesis of the hydroxyl end-member of humite, $Mg_2Si_3O_{12}(OH)_2$. Am Mineral, 80: 638-640.

Xia, X., and Weidner, D.J., and Zhao, H. (1998) Equation of state of brucite: single-crystal Brillouin spectroscopy study and polycrystalline pressure-volume-temperature measurements. Am Mineral, 83, 68-74.

Yamamoto, K. (1977) The crystal structure of hydroxyl-chondrodite. Acta Crystallogr, B33: 1481-1485.

Ye, Y., Schwering, R.A., and Smyth, J.R. (2009) Effects of hydration on thermal expansion of forsterite, wadsleyite, and ringwoodite at ambient pressure. Am Mineral, 94: 899-904.

Ye, Y., Smyth, J.R., Jacobsen, S.D., and Goujon, C. (2013) Crystal chemistry, thermal expansion, and Raman spectra of hydroxyl-clinohumite: implications for water in Earth's interior. Contrib Mineral Petrol, 165: 563-574.

Zha, C.-S., Duffy, T.S., Downs, R.T., Mao, H.-k., and Hemley, R.J. (1996) Sound velocity and elasticity of single-crystal forsterite to 16 GPa. J Geophys Res, 101(B8): 17,535-17,545.

Zha, C.-S., Duffy, T.S., Downs, R.T., Mao, H.-k., and Hemley, R.J. (1998) Brillouin scattering and X-ray diffraction of San Carlos olivine: direct pressure determination to 32 GPa. Earth Planet Sci Lett, 279: 11-19.

546 **Figure Captions**

547 **Fig. 1** Composition of hydrous magnesium silicates in the hydrous peridotite system (MgO-SiO_2-
548 $Mg(OH)_2$). A: phase A; Nrb: Norbergite; Chn: chondrodite; Hu: humite; Chu: clinohumite; Fo: Forsterite;
549 En: enstatite; B: phase B; Ahy B: anhydrous phase B; Shy B: supper hydrous phase B; Tlc: talc; Ant:
550 antigorite; E: Phase E (non-stoichiometric, Si/Mg 1.8~2.1, C_{H2O} 6~18 wt%); D: Phase D (Si/Mg 0.5~0.8,
551 C_{H2O} 13~19 wt%); 10 Å (C_{H2O} 7~13 wt%); Hy Wad: hydrous wadsleyite (C_{H2O} up to 3.3wt%).

552 **Fig. 2.** Crystal structure of OH-chondrodite viewed down the *a* axis, with hydrogen positions shown as
553 black spheres. M1-M3 refer to (Mg,Fe) octahedra, and the silicate tetrahedron is labeled Si.

554 **Fig. 3** Unpolarized Raman spectra of the three OH-chondrodite crystals used in the Brillouin scattering
555 experiments: **(A)** low-wavenumber region, **(B)** mid-wavenumber region, **(C)** high-wavenumber region
556 showing O-H stretching bands, **(D)** high-wavenumber region of one sample shown with the two main O-H
557 stretching bands deconvolved into six different components (dashed lines), sum of the fitted peaks (solid
558 line) and spectral data points (grey dots). The unpolarized Raman spectra were collected in backscatter
559 geometry with the incident laser perpendicular to each plane expressed as (*hkl*), fitted by Brillouin
560 spectroscopy.

561 **Fig. 4. (A-C).** Longitudinal acoustic (LA) and transverse acoustic (TA) velocities in three different planes
562 (*hkl*) of OH-chondrodite as a function of crystallographic direction. The azimuthal angle is relative to an
563 arbitrary starting angle. The solid curves were calculated using the best fit elastic constants for comparison
564 with the measured velocities (filled circles).

565 **Fig. 5. (A)** Unit-cell volume and principal expansion axes of OH-chondrodite as a function of temperature
566 between 153 and 787 K. The solid curves are fitting to the data normalized to 153 K, using the Fei
567 equation. Experimental uncertainties are smaller than the size of the symbols. **(B)** Volumetric thermal
568 expansion coefficient as a function of temperature from Fei, Suzuki and Kumar equations, which are
569 extrapolated to 1500 K.

570 **Fig. 6.** The average thermal expansion coefficients as a function of water content for DHMS phases along
571 the forsterite-brucite join. The temperature ranges are 300 – 787 K for forsterite (Fo, Ye et al. 2009),
572 clinohumite (Chu, Ye et al. 2013), and chondrodite (Chn, this study); 293 – 873 K for phase A (PhA,
573 Pawley et al. 1995); 299 – 593 K for brucite (Bru, Fukui et al. 2003).

574 **Fig. 7**. Unit-cell volumes of Fe-free OH-Chondrodite samples (Ross and Crichton 2001; Kuribayashi et al.
575 2001) as a function of pressure, with 3rd-order Birch-Murnaghan Equation of State (BM EoS) fitting. The
576 volumes are normalized to their respective V_0 values at ambient conditions.
577 **Fig. 8.** Elastic properties of DHMS along the forsterite-brucite join: **(A)** density as a function water content,
578 **(B)** bulk modulus (K_0) and shear modulus (G_0) as a function of water content, **(C)** compressional (V_P) and
579 shear-wave (V_S) velocities as a function of water content. Linear fits to the data (dashed lines) are given in
580 the text (equations 13-17). References are given in Table 9.
581

Table 1. Thermoelastic properties of Phase A, chondrodite and clinohumite (F-free) at ambient conditions.

	Phase A	Chondrodite	Clinohumite
Formula	$Mg_7Si_2O_{14}H_6$	$Mg_5Si_2O_{10}H_2$	$Mg_9Si_4O_{18}H_2$
C_{H2O} (wt%)	11.8	5.4	2.9
ρ (g/cm^3)	2.949(1)[a]	3.099(1)[b]	3.134(1)[c]
α_0 (10^{-6} K^{-1})	46(2)[d]	38.0(9)[b]	36.8(6)[c]
K_{S0} (GPa)	100(1)[e]	118(1)[b]	119(2)[e]
G_0 (GPa)	61(1)[e]	70.1(5)[b]	77(1)[e]
V_P (km/s)	7.84(8)[e]	8.26(8)[b]	8.41(9)[e]
V_S (km/s)	4.55(7)[e]	4.76(4)[b]	4.96(8)[e]
K_{T0} (GPa)	97.5(4)[a]	114(1)[b]	119.4(7)[f]
K_T'	6.0(1)[a]	5.5(1)[f]	4.8(2)[f]
C_P (J·kg^{-1}·K^{-1})	924(1)[g]	874(1)[g]	884(1)[h]
Θ_{ac} (K)[i]	726(13)	741(10)	760(15)
γ[i]	1.69(8)	1.66(4)	1.50(4)

a: Crichton and Ross (2002); *b*: This study; *c*: Ye et al. (2013); *d*: Pawley et al. (1995); *e*: Phan (2009); *f*: refined on the data from Ross and Crichton (2001) and Kuribayashi et al. (2004); *g*: Cynn et al. (1996); *h*: Holland and Powell 1998. *i*; the Debye temperatures and Grüneisen parameters are calculated in this study.

Table 2. Composition of OH-chondrodite SZ0407B from electron microprobe analyses.

	wt%		apfu[#]		wt%		apfu
SiO_2	34.09(6)	Si	1.945(3)	NiO	0.04(1)	Ni	0.0018(5)
TiO_2	0.003(3)	Ti	0.0001(1)	MnO	0.008(3)	Mn	0.0004(1)
Al_2O_3	0.026(3)	Al	0.0017(2)	CaO	0.014(3)	Ca	0.0008(2)
MgO	59.34(5)	Mg	5.047(4)	H_2O[$]	5.26	H	2
FeO	1.22(3)	Fe	0.058(2)	Total	100.00(6)		

#: atoms per formula unit.
$: The wt% and apfu values for H_2O/H are calculated from stoichiometry, assuming that the molar ratio of H:O is 2:10.

Table 3. Atomic positions and occupancy factors from X-ray intensity scan (space group: $P2_1/b$).

Atom	*x*/*a*	*y*/*b*	*z*/*c*	occupancy
M1	0.5	0	0.5	Mg: 0.991(2) / Fe: 0.009(2)
M2	0.00761(6)	0.17542(3)	0.30892(4)	Mg: 0.992(2) / Fe: 0.008(2)
M3	0.48780(6)	0.88398(3)	0.07707(4)	Mg: 0.989(2) / Fe: 0.011(2)
Si	0.07769(4)	0.14073(2)	0.70194(2)	0.983(2)
O1	0.77577(11)	0.00294(5)	0.29661(7)	1
O2	0.72759(11)	0.24411(5)	0.12853(7)	1
O3	0.22561(11)	0.16797(5)	0.52799(7)	1
O4	0.26251(11)	0.85683(5)	0.29738(7)	1
O5	0.26372(14)	0.06017(6)	0.10540(9)	1
H	0.109(3)	0.046(2)	0.004(3)	1

Table 4. Bond lengths (Å) and polyhedral volumes (Å^3).

M1		**M2**		**M3**	
O1×2:	2.0805(5)	O1:	2.0713(6)	O1:	2.2413(6)
O3×2:	2.1253(5)	O2:	2.2257(6)	O2:	2.0140(6)
O4×2:	2.1227(5)	O3:	2.0387(6)	O2:	2.1123(6)
Avg. bond:	2.1095(5)	O3:	2.1772(6)	O4:	2.1363(6)
Poly. V (Å^3):	12.04(1)	O4:	2.1983(6)	O5:	2.0604(7)
		O5:	2.0630(7)	O5:	2.0819(7)
Si		Avg. bond:	2.1290(7)	Avg. bond:	2.1077(7)
O1:	1.6461(6)	Poly. V (Å^3):	12.47(1)	Poly. V (Å^3):	12.13(1)
O2:	1.6427(6)				
O3:	1.6463(6)	**H**			
O4:	1.6151(6)	O5:	1.06(2)		
Avg. bond:	1.6376(6)				
Poly. V (Å^3):	2.22(1)				

Table 5. Selected bond length (Å) for chondrodite samples from this and previous studies.

	Fe %*	F %+	Ti %*	α (°)	V (Å^3)	M2-OF5	M3-OF5$_1$	M3-OF5$_2$
SZ0407B$	1.1	0	0	108.702(7)	367.50(4)	2.0628(5)	2.0599(6)	2.0825(6)
Y77$	0	0	0	108.71(5)	368.7(2)	2.133(3)	2.056(3)	2.091(3)
B02	1.4	77	0	109.11(1)	357.26(3)	2.054(8)	2.011(8)	2.015(9)
G70	1	65	0	109.059(2)	359.30(1)	2.045(2)	2.016(1)	2.042(2)
O00	0.8	62	0	109.08(2)	359.47(1)	2.051(3)	2.019(3)	2.045(3)
F01&	5.6	51	0.46	109.097(2)	363.14(4)	2.060(1)	2.033(1)	2.059(1)
F02&	5.6	58	0.46	109.065(1)	361.98(2)	2.057(8)	2.01(1)	2.055(9)
K06&	5.6	58	0.46	109.065(3)	361.98(2)	2.068(5)	2.048(5)	2.067(5)
K04&	4.4	37	0.4	109.07(1)	361.0(2)	2.057(1)	2.024(2)	2.053(1)
F78	12.5	0	8.4	109.33(1)	363.83(5)	2.051(2)	1.976(2)	1.987(2)

SZ0407B: this study; Y77: Yamamoto (1977); B02: Berry and James (2002); G70: Gibbs et al. (1970); O00: Ottolini et al. (2000); F01: Friedrich et al. (2001); F02: Friedrich et al. (2002); K06: Kunz et al. (2006); K04: Kuribayashi et al. (2004): F78: Fujino and Takéuchi (1978).
*: Atomic percentage in the total metallic cations.
+: Molar ratio of F/(F+OH).
$: synthesized from experiments, while others are from natural sources.
&: data measured at ambient condition.

Table 6. Average thermal expansion coefficients for the unit-cell parameters and the principal expansion axes (153 – 787 K), and the orientations of the principal axes.

Unit-cell parameters		Principal expansion axes		orientations		
	α_0 (10^{-6} K^{-1})		α_0 (10^{-6} K^{-1})	***a***	***b***	***c***
a	12.7(3)	$\boldsymbol{X_1}$	12.7(3)	1	0	0
b	11.5(2)	$\boldsymbol{X_2}$	10.6(2)	0	0.8353	0.5499
c	14.6(4)	$\boldsymbol{X_3}$	14.7(4)	0	-0.1636	0.9865
α	1.43(10)					
V	38.0(9)					

Table 7. Single-crystal elastic constants (in GPa) for chondrodite at ambient conditions.

	This study	SB89		This study	SB89
longitudinal			off-diagonal		
$C_{11}(C_{33})$	188.0(7)	213.4(15)	$C_{12}(C_{13})$	61(10)	70(3)
$C_{22}(C_{11})$	278.0(10)	275.3(15)	$C_{13}(C_{23})$	71.4(7)	59(2)
$C_{33}(C_{22})$	195.7(7)	198.4(12)	$C_{23}(C_{12})$	74(3)	67(3)
shear			$C_{15}(C_{14})$	3.9(4)	7.2(10)
$C_{44}(C_{66})$	64.0(10)	69.7(6)	$C_{25}(C_{24})$	2.6(10)	-1.7(12)
$C_{55}(C_{44})$	68.3(4)	72.1(9)	$C_{35}(C_{34})$	2.5(4)	-2.6(8)
$C_{66}(C_{55})$	71.3(5)	75.2(7)	$C_{46}(C_{56})$	4.1(6)	-0.7(4)

SB89:: Sinogeikin and Bass (1999).
The elastic constants are given in the standard monoclinic coordinate system (*b*-unique, $P2_1/c$), while the values inside parentheses are those for an *a*-unique coordinate system ($P2_1/b$).

Table 8. Aggregate elastic moduli and pressure derivative of bulk modulus for chondrodite

	F/(F+OH)	Fe (mol%)	K_{T0} (GPa)	K_T'	G_0 (GPa)
This study	0	1.1	119.4[&]		71.1 (Voigt bound)
			116.4[&]		69.2 (Reuss bound)
			117.9(12)[&]		70.1(5) (VRH average)
			114.2[+]	5.5(1)[#]	
Sinogeikin and Bass (1999)	0.32	5.5	118.4(16)[&]		75.6(7)
Ross and Crichton (2001)	0	0	115.7(8)	4.9(2)	
Kuribayashi et al. (2004)	0	0	117(2)	4[*]	
Kuribayashi et al. (2004)	0.37	4.4	124.1(4)	4[*]	
Friedrich et al. (2002)	0.55	0	117(4)	5.6(1)	
Faust and Knittle (1994)	0.69	0	136.2	3.7[*]	

&: adiabatic bulk modulus.
+: K_{T0} calculated from Reuss bound K_{S0}.
#: Refined on the datasets of Ross and Crichton (2001) and Kuriyabashi et al. (2004), with K_{T0} = 114.2 GPa.
*: fixed without refinement.

Table 9. Studies of elasticity for DHMS along the olivine-brucite join, listed in the order of H_2O content increasing.

	H_2O (wt%)	density (g/cm^3)	Fe (mol%)	K_{S0} (GPa)	G_0 (GPa)	V_P (km/s)	V_S (km/s)
Olivine:							
Suzuki et al. (1983)	0	3.225(1)	0	128.9(2)	81.4(2)	8.58(1)	5.02(1)
Zha et al. (1996)	0	3.221(1)	0	128.8(5)	81.6(2)	8.59(3)	5.03(1)
Webb (1989)	0	3.350(1)	10	129.5(2)	77.5(2)	8.34(1)	4.81(1)
Zha et al. (1998)	0	3.343(1)	10	131.1(19)	79.4(8)	8.42(9)	4.87(4)
Jacobsen et al. (2008, 2009)	0.8	3.240(1)	3	125.2(2)	77.7(1)	8.40(1)	4.90(1)
Jacobsen et al. (2008, 2009)	0.9	3.180(1)	0	125.4(4)	79.6(3)	8.53(2)	5.00(2)
Clinohumite:							
Fritzel and Bass (1997)	2.0[a]	3.261(1)	6.5	125(2)	73(5)	8.26(9)	4.7(3)
Phan (2009)	2.9	3.134(1)	0	119(2)	77(1)	8.41(9)	4.96(8)
Chondrodite:							
Sinogeikin and Bass (1999)	3.3[b]	3.227(1)	9.4	118(2)	75.6(7)	8.24(8)	4.84(5)
This study	5.3	3.099(1)	1.1	118(1)	70.6(5)	8.26(8)	4.76(4)
Phase A:							
Sanchez-Valle et al. (2008)	11.7	2.976(1)	1.9	106(1)	61(1)	7.93(8)	4.53(8)
Phan (2009)	11.8	2.949(1)	0	100(2)	61(1)	7.84(9)	4.55(8)
Brucite:							
Jiang et al. (2006)	30.9	2.380(1)	0	43.8(8)	35.2(3)	6.2(1)	3.85(3)
Xia et al. (1998)	30.9	2.380(1)	0	46(1)	34.9(5)	6.2(1)	3.83(5)

a: F/(F+OH) = 0.29 for clinohumite; *b*: F/(F+OH) = 0.32 for chondrodite.

Appendix 1. Anisotropic displacement parameters (Å^2).

Atom	U_{11}	U_{22}	U_{33}	U_{23}	U_{13}	U_{12}	U_{eq}
M1	0.0058(2)	0.0069(2)	0.0061(2)	0.0014(1)	0.0009(1)	0.0005(1)	0.0064(1)
M2	0.0085(2)	0.0065(2)	0.0071(2)	0.0029(1)	-0.0004(1)	0.0004(1)	0.0072(1)
M3	0.0072(1)	0.0094(2)	0.0074(1)	0.0040(1)	-0.0004(1)	0.0004(1)	0.0077(1)
Si	0.0042(1)	0.0056(1)	0.0054(1)	0.0022(1)	0.0000(0)	0.0000(0)	0.0050(1)
O1	0.0074(2)	0.0065(2)	0.0084(2)	0.0030(1)	0.0005(2)	-0.0001(1)	0.0073(1)
O2	0.0068(2)	0.0074(2)	0.0070(2)	0.0015(2)	0.0002(1)	-0.0001(1)	0.0073(1)
O3	0.0066(2)	0.0082(2)	0.0065(2)	0.0035(1)	0.0002(1)	-0.0001(1)	0.0068(1)
O4	0.0043(2)	0.0084(2)	0.0075(2)	0.0027(2)	0.0001(1)	0.0000(1)	0.0067(1)
O5	0.0189(3)	0.0100(2)	0.0202(3)	0.0080(2)	0.0127(2)	0.0059(2)	0.0156(1)
H							0.054 (fixed)

Appendix 2. Unit-cell parameters of chondrodite as functions of temperature, as well as the principle expansion axes, which are normalized to the ones at 153 K

T (K)	a (Å)	b (Å)	c (Å)	α (°)	V (Å^3)	X_1/X_{10}	X_2/X_{20}	X_3/X_{30}
153(2)	4.7402(3)	10.3341(8)	7.8899(8)	108.687(8)	366.12(4)	1	1	1
203(2)	4.7419(3)	10.3387(8)	7.8926(8)	108.693(8)	366.53(4)	1.00036	1.00030	1.00045
253(2)	4.7438(3)	10.3439(7)	7.8969(7)	108.698(7)	367.04(4)	1.00078	1.00076	1.00099
300(2)	4.7459(2)	10.3480(7)	7.9002(7)	108.702(7)	367.50(4)	1.00120	1.00114	1.00142
350(3)	4.7489(2)	10.3530(7)	7.9052(7)	108.706(8)	368.13(4)	1.00183	1.00164	1.00201
396(3)	4.7516(2)	10.3583(7)	7.9105(8)	108.708(9)	368.77(4)	1.00240	1.00217	1.00266
443(3)	4.7546(2)	10.3637(7)	7.9168(7)	108.715(9)	369.47(4)	1.00304	1.00267	1.00344
495(4)	4.7578(2)	10.3695(7)	7.9226(8)	108.722(9)	370.18(4)	1.00371	1.00318	1.00418
544(4)	4.7610(2)	10.3771(7)	7.9286(7)	108.735(9)	370.95(5)	1.00439	1.00380	1.00498
587(4)	4.7640(2)	10.3827(8)	7.9345(8)	108.737(8)	371.67(5)	1.00502	1.00435	1.00571
635(5)	4.7674(3)	10.3892(8)	7.9403(9)	108.750(9)	372.41(6)	1.00574	1.00486	1.00648
685(5)	4.7704(3)	10.3951(8)	7.9470(9)	108.764(9)	373.14(6)	1.00637	1.00534	1.00734
736(6)	4.7738(3)	10.4022(8)	7.9545(9)	108.771(9)	373.99(6)	1.00709	1.00599	1.00829
787(6)	4.7773(3)	10.4099(8)	7.9619(9)	108.795(9)	374.84(6)	1.00783	1.00653	1.00929

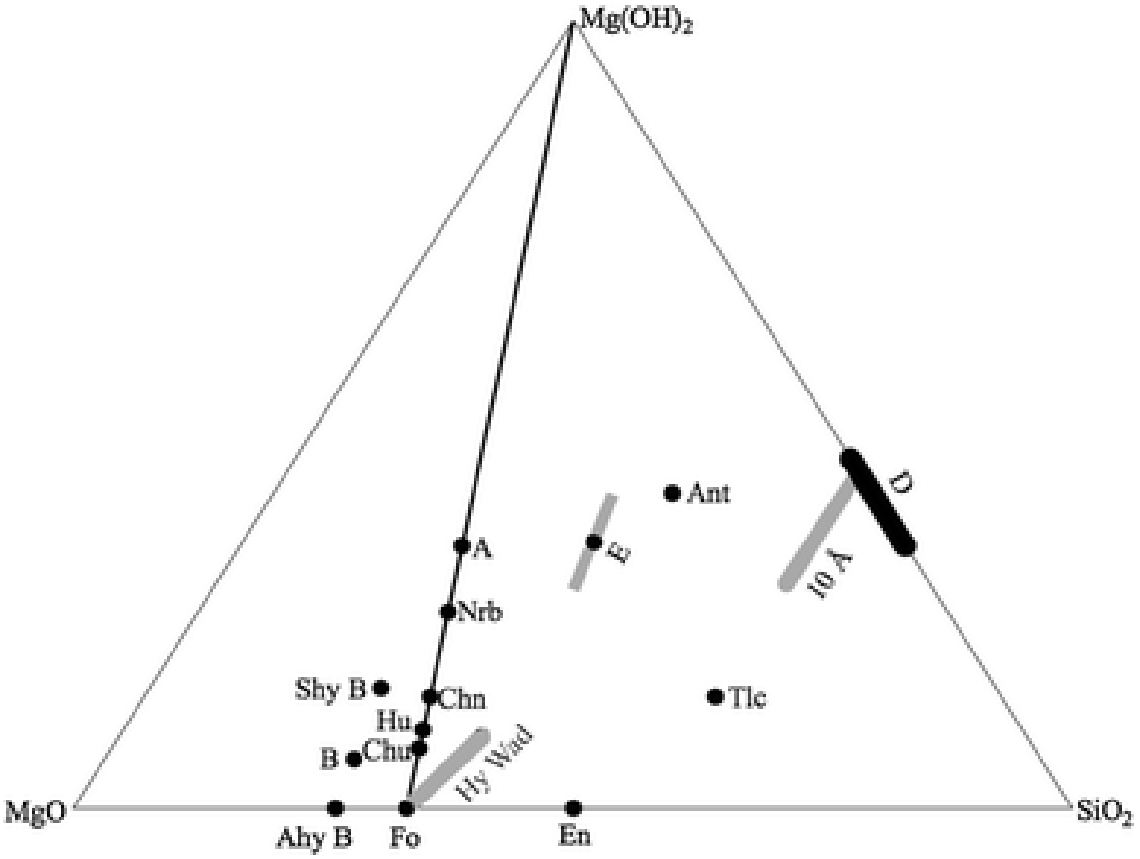

Figure 1.

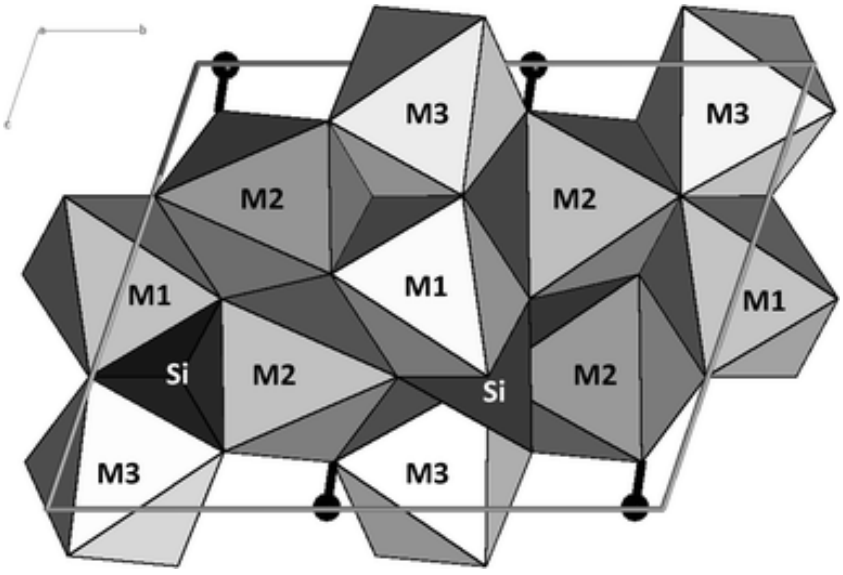

Figure 2.

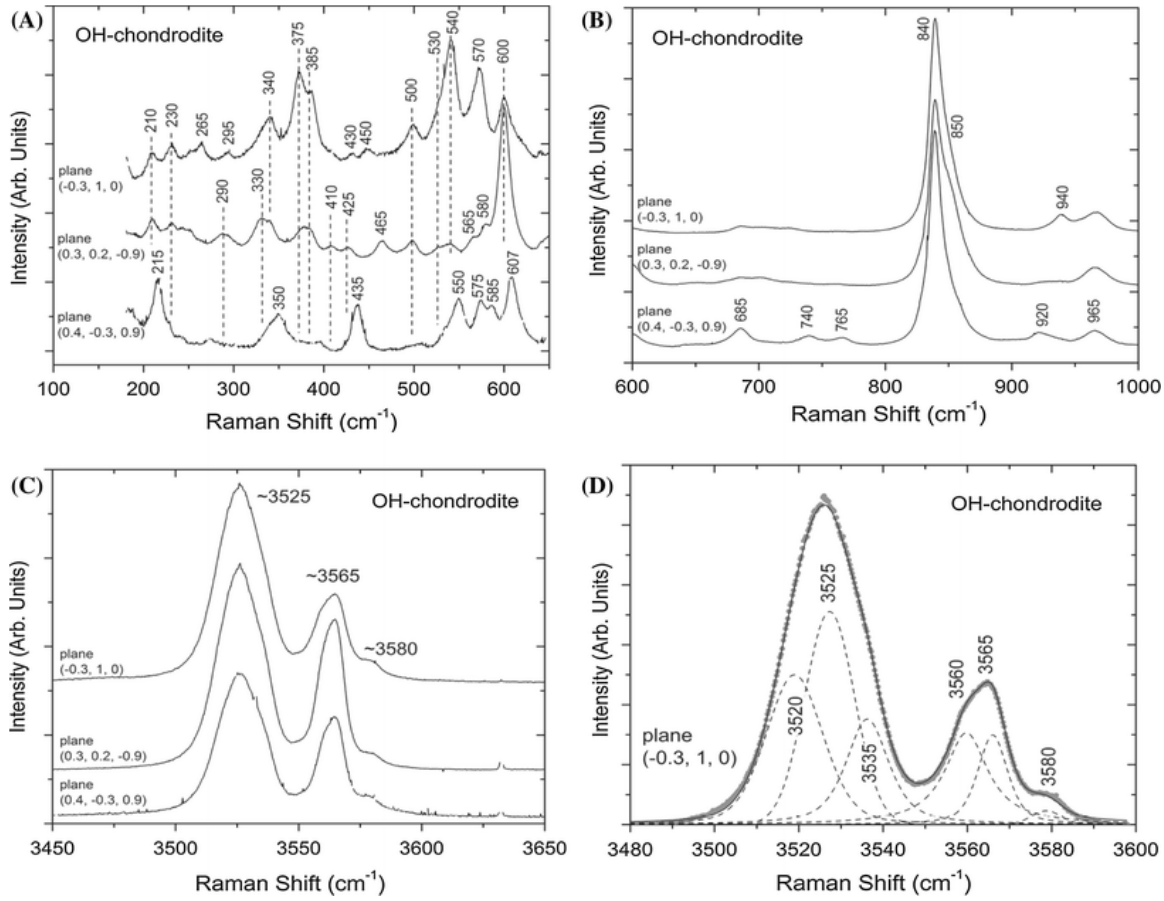
(A)
OH-chondrodite
Intensity (Arb. Units)
Raman Shift (cm-1)
plane (-0.3, 1, 0)
plane (0.3, 0.2, -0.9)
plane (0.4, -0.3, 0.9)
210
230
265
295
340
375
385
430
450
500
530
540
570
600
290
330
410
425
465
565
580
215
350
435
550
575
585
607
(B)
OH-chondrodite
840
850
940
685
740
765
920
965
(C)
~3525
~3565
~3580
(D)
3520
3525
3535
3560
3565
3580

Figure 3.

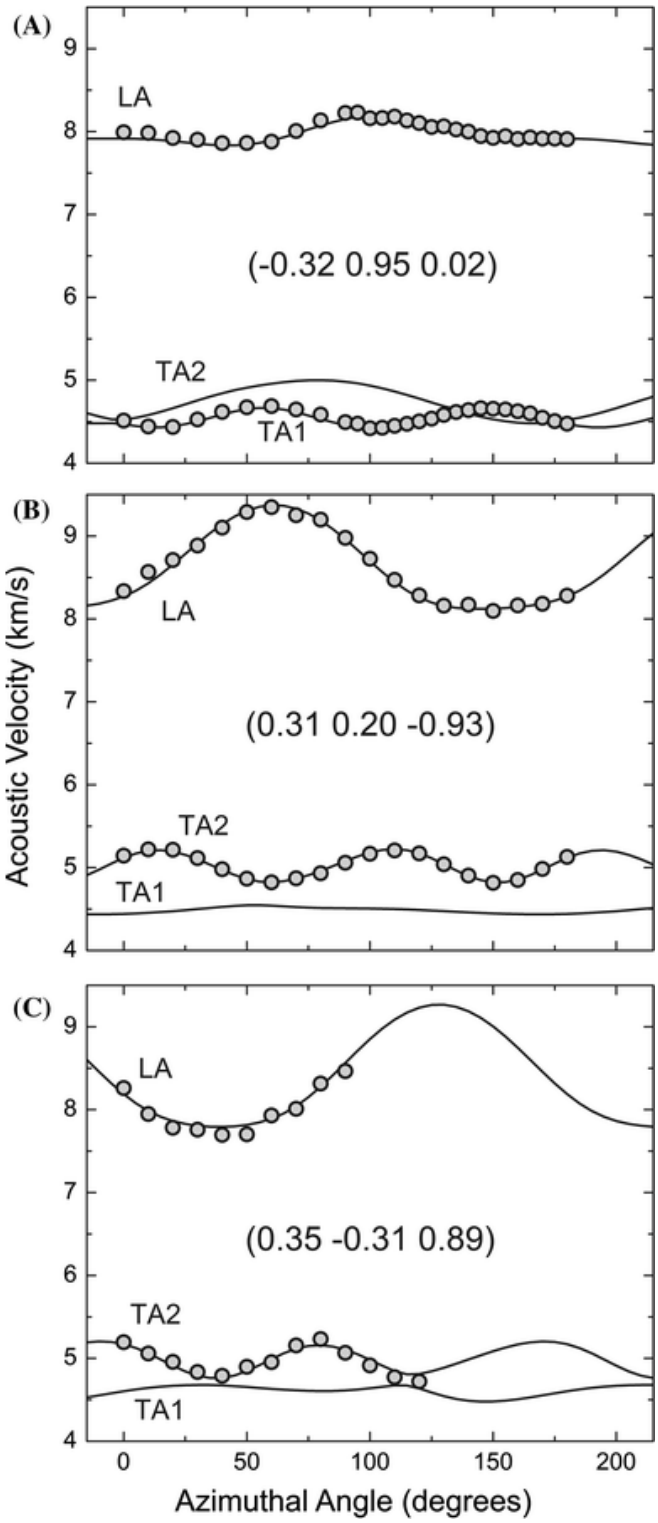

785
786 Figure 4.

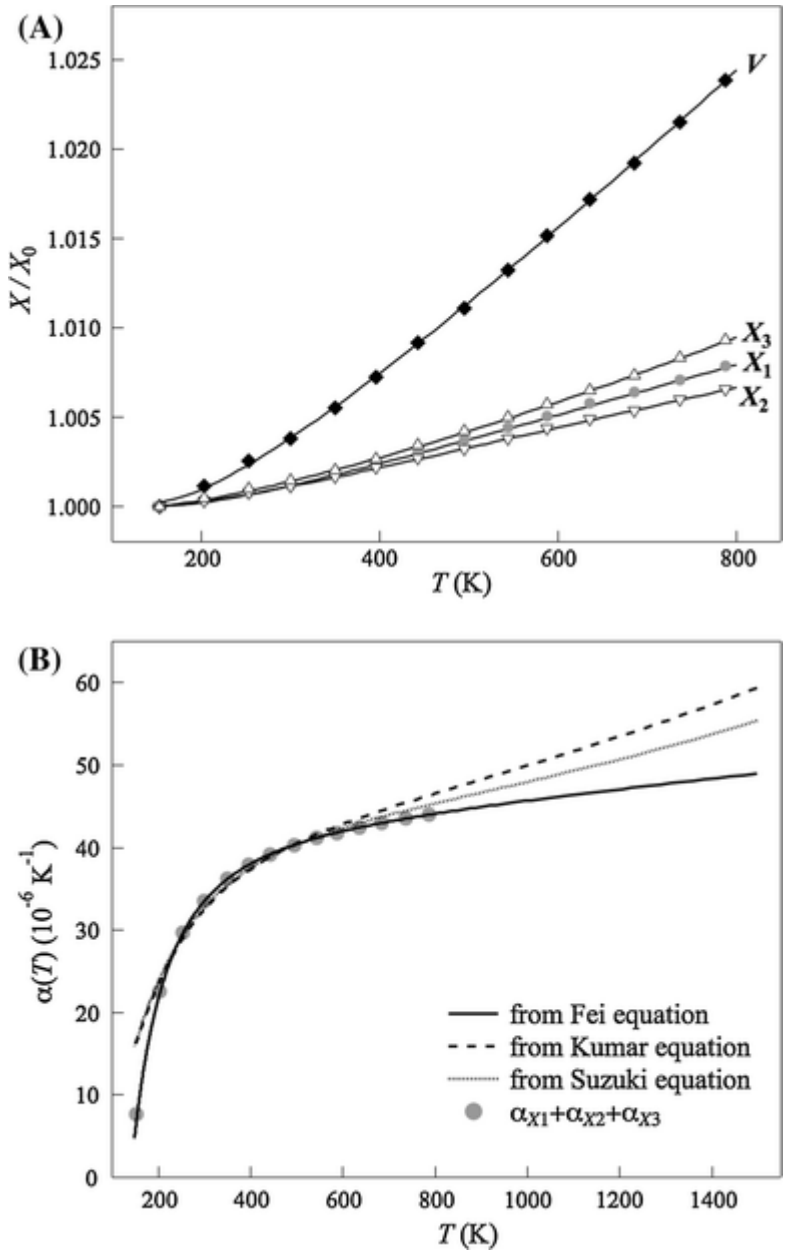

787
788
789 Figure 5.

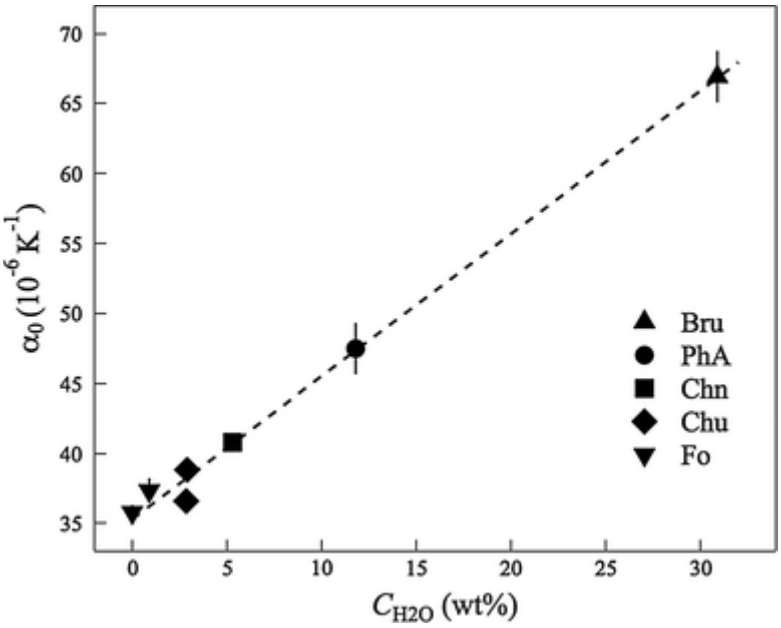

790
791
792 Figure 6.
793
794

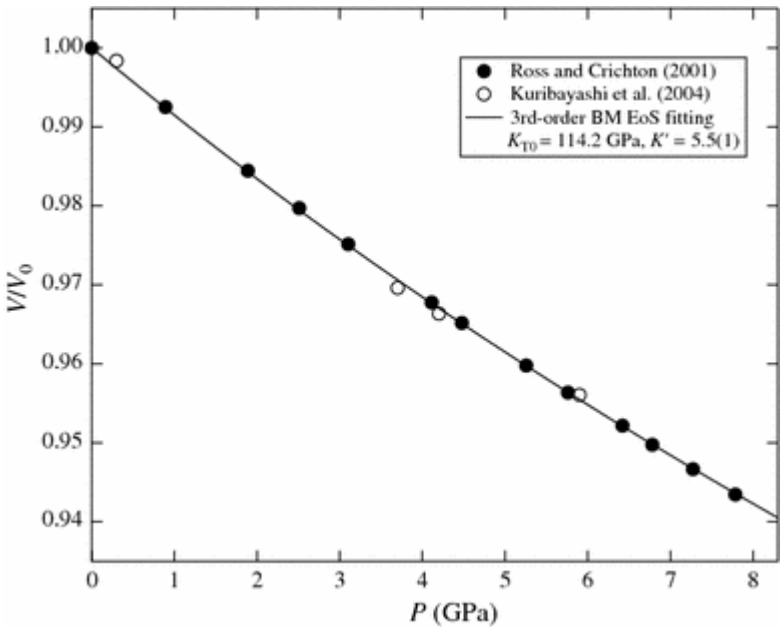

795
796
797 Figure 7.

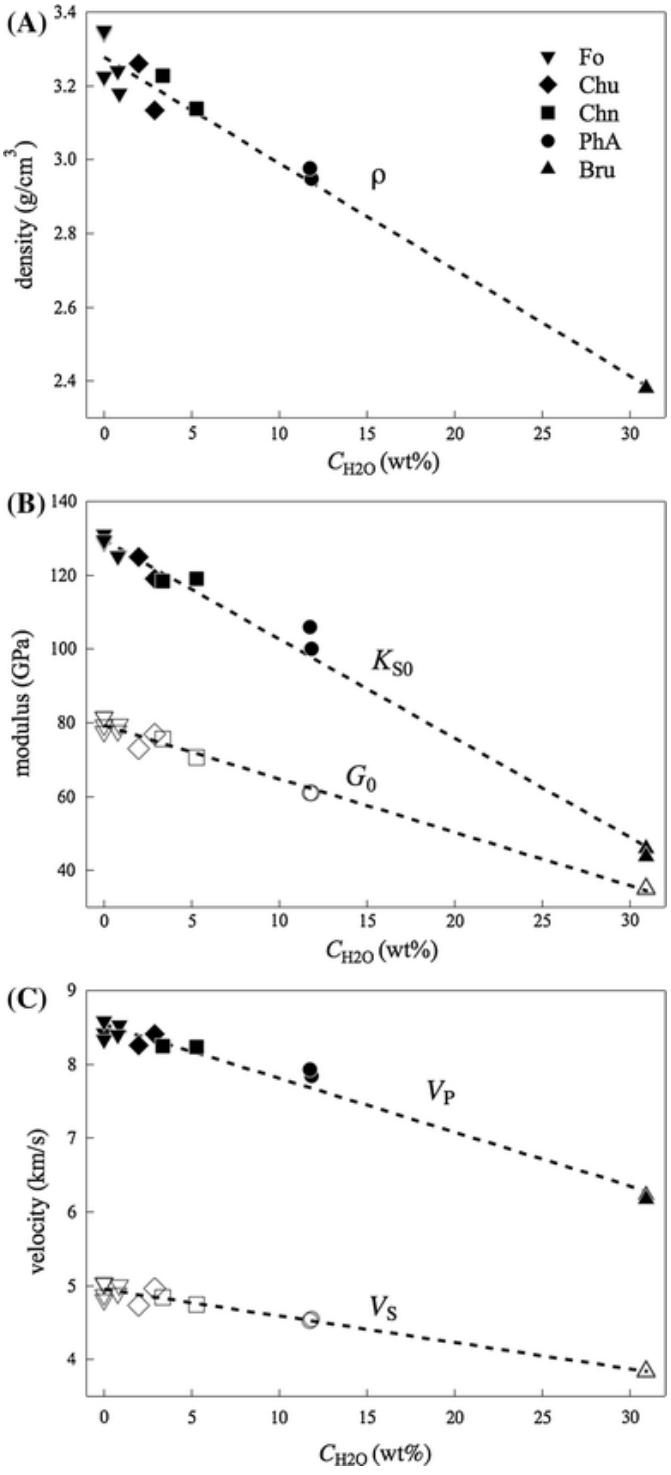

798
799
800 Figure 8.